Materials Advances

ROYAL SOCIETY OF CHEMISTRY

PAPER

View Article Online
View Journal | View Issue

Cite this: *Mater. Adv.*, 2026, 7, 4848

Dual redox-active bi-metallic oxide/nanoporous carbon nanotube hybrid architectures: probing diffusion dynamics and ionic conductivity for advanced supercapacitors

Muhammad Luqman, †*[a] Muhammad Mehak,†[a] Muhammad Umar Salman, [a] Umair Ali,[b] Shahid M. Ramay,[c] M. Younis[d] and Shahid Atiq *[a]

Received 1st March 2026,
Accepted 19th March 2026

DOI: 10.1039/d6ma00284f

rsc.li/materials-advances

Growing demand for sustainable energy storage drives the development of advanced materials and porous structures. Here, $CrCo_2O_4$ (CCO) and its composites with varying carbon-nanotube (CNT) content (3, 6, and 9%) are synthesized, termed as CCO-3%, CCO-6% and CCO-9%. X-ray diffraction confirms the spinel phase of CCO, while the morphology reveals higher CNT content, enhancing surface porosity. A cyclic voltammetry study demonstrates a battery-type hybrid charge storage mechanism, as evident by Dunn's model. Among these composites, CCO-9% exhibits the highest performance, achieving an impressive specific capacity (Q_{sp}) of 817.30 C g^{-1} at 1.3 A g^{-1}. It delivers an energy density (E_d) of 56.75 Wh kg^{-1} along with a power density (P_d) of 338.98 W kg^{-1}. The galvanostatic intermittent titration technique reveals the highest value of diffusion coefficient, $\sim 2.65 \times 10^{-10}$ cm^2 s^{-1}, while electrochemical impedance spectroscopy reveals a reduced charge transfer resistance and an improved ionic conductivity of 4.02×10^{-4} S cm^{-1}. The electrode is utilized in an asymmetric device, where testing reveals a Q_{sp} of 129.48 C g^{-1}, corresponding to an E_d of 21.58 Wh kg^{-1} at a P_d of 1016.94 W kg^{-1}. The electrode displays remarkable cycling stability, sustaining 98% of its initial capacity after 10k cycles. These results highlight CCO-9% as a viable contender for hybrid capacitors, portable electronic devices and regenerative braking systems.

1. Introduction

Escalating global demand, driven by continuous technological innovation and industrial expansion, has placed unprecedented pressure on conventional energy systems. Simultaneously, critical issues such as climate change, unsustainable resource consumption and the depletion of fossil fuel reserves have emerged as formidable challenges, necessitating the development of clean, efficient and renewable energy alternatives.[1,2] Renewable energy resources have gained attention as scalable, flexible, and sustainable energy options. As a result, researchers are shifting their focus toward developing more efficient, environmental friendly, and cost-effective energy storage systems, such as fuel cells, batteries, and supercapacitors (SCs).[3,4] Among these energy storage devices (ESDs), SCs have gathered considerable attention due to their advantages over fuel cells, which offer limited lifespans, and batteries, which are prone to degradation and low power density (P_d). SCs provide rapid charge–discharge cycles, low internal resistance, and straightforward setup, rendering them highly adaptable for versatile practical applications. They have been progressively used in electronic devices, including power tools, electric vehicles, smart sensors, robotics, and memory backup systems.[5–7] Their high P_d, flexibility, durability and cost-effectiveness further enhance their appeal.[8]

SCs are regarded as a unique class of ESDs that combine the rapid power delivery of capacitors with the enhanced energy storage capacity characteristics of batteries. Despite their many advantages, the relatively low energy density (E_d) of SCs is a limitation. To address this issue, researchers are focusing on the enhancement of E_d by designing porous nanostructures and nano-composites while preserving high P_d.[9,10] Critical factors influencing the charge storage performance of SCs include surface area, porosity, and electrical conductivity. The choice of electrode material plays a decisive role in improving the electrochemical (EC) performance and efficiency of SCs. Promising materials such as metal–organic frameworks

[a] *Centre of Excellence in Solid State Physics, University of the Punjab, Lahore-54590, Pakistan. E-mail: muhammadluqman00100@gmail.com, satiq.cssp@pu.edu.pk*
[b] *Additive Manufacturing Institute, Shenzhen University, Shenzhen 518060, China*
[c] *Physics and Astronomy Department, Faculty of Science, King Saud University (KSU), Riyadh, Saudi Arabia*
[d] *College of Physics and Optoelectronic Engineering, Shenzhen University, Shenzhen 518060, China*
† Authors contribute equally.

(MOFs), conducting polymers, and transition metal sulfides and oxides (TMOs) have shown significant potential in this regard.[11,12]

MOFs and conducting polymers offer very low conductivity and inherent mechanical stability problems, while TMOs employed as an electrode material for SCs are abundant, non-toxic in nature, chemically stable and easy to prepare.[13,14] Flexible redox mechanisms owing to multiple oxidation states make TMOs a promising candidate for the development of efficient SC materials, *i.e.* $FeCo_2O_4$, $NiMn_2O_4$, $MnCo_2O_4$, and $NiCo_2O_4$.[15,16]

From the aforementioned materials, Li *et al.* studied the morphology-dependent EC properties of $FeCo_2O_4$ *via* a wet chemical technique. The microflower-like morphology exhibited higher EC features over micro particles. The highest specific capacitance (C_s) was found for the flower-like morphology at about 301 F g^{-1} at a current density (J) of 1 A g^{-1}, with 99.3% specific retention.[17] Likewise, a $NiCo_2O_4$ microsphere material was fabricated by Yang *et al. via* the EC deposition method, which demonstrated brilliant C_s of 379.4 mF cm^{-2} at J of 1.5 mA cm^{-2} with 87.1% retention rate.[18] Additionally, a C_{sp} of 762 F g^{-1} at a J of 1 A g^{-1} was calculated for the $NiMn_2O_4$ composite, which was prepared by Dhas *et al.* Consequently, the material manifested an excellent E_d of 11.9 Wh kg^{-1} at a P_d value of 44.4 kW kg^{-1}.[19] Furthermore, the urchin-like morphology of the $MnCo_2O_4$ nano-spheres, which were prepared by Shen *et al.*, provided an exceptional C_{sp} value of 2019 F g^{-1} at a J of 1 A g^{-1}, and after 10k cycles the composite maintained 96% capacitance at an E_d of 69.0 Wh kg^{-1} and a P_d of 793 W kg^{-1}.[20]

TMOs offer poor cycling stability due to phase transitions and surface lattice degradation induced by continuous charge–discharge cycles.[21] $CrCo_2O_4$ (CCO), a spinel-structured TMO, presents a viable strategy to enhance EC performance by providing an expanded surface area, superior electrical conductivity, and enhanced structural stability. As an electrode material, CCO, particularly at elevated chromite concentrations, exhibits exceptional corrosion inhibition properties. Structurally, it adopts a spinel configuration, wherein Cr^{2+} ions occupy tetrahedral sites while Co^{3+} ions reside in octahedral coordination.[22] Despite its potential as a promising electrode candidate for SC applications, CCO faces challenges related to fabrication complexity, stability, and catalytic efficiency.

To overcome these limitations, hybrid composites with CNTs can induce synergistic effects, thereby augmenting EC efficacy for commercial viability. Additionally, nano-architectures, including nanotubes, nanowires, and multilayered arrays, offer significantly increased surface area, enhanced charge storage capacity, and improved long-term stability.[23] This strategic integration accelerates the charge transfer kinetics, thereby facilitating superior rate capability, which is crucial for high-energy storage applications.[24]

To the best of our knowledge, a detailed investigation into the charge storage mechanism of CCO with this strategic integration has not yet been studied. Owing to their remarkable electrical conductivity, large surface area, and efficient ion transport capabilities, CNTs have attracted considerable interest for energy storage applications. Consequently, incorporating CNTs into the CCO framework is expected to significantly enhance their EC performance. The objective of this study is to reinforce varying weight fractions of CNTs (0, 3, 6, and 9%) into the CCO matrix to optimize its EC performance. Particular emphasis is placed on improving ionic transport and diffusion kinetics, as well as retaining structural stability under repeated charge–discharge cycles. To investigate the diffusion kinetics, this study uniquely employs the galvanostatic intermittent titration technique (GITT). Initially, pure-phase CCO was synthesized *via* a hydrothermal method, and then CNT-integrated CCO composites were fabricated using a solvothermal technique. These composites are named CCO, CCO-3%, CCO-6% and CCO-9% for our convenience. These composite formulations were subsequently employed in the fabrication of the electrodes and later analyzed to explore the underlying charge storage mechanisms.

2. Synthesis methodology and electrode fabrication

2.1 Synthesis of CCO materials

A hydrothermal method was employed to synthesize the facile materials. To follow through on that, chromium (Cr) and cobalt (Co) metal precursors in the form of nitrates were taken in the appropriate molar ratios. Stoichiometric calculations were carried out to make a total mass of 5 g of the precursors. These metal nitrates were solubilized in 50 mL of deionized water (DIW), together with urea and ammonium fluoride in a 2 : 1 ratio. 5 mL of ethylene glycol was added to the solution as a stabilizing agent. The mixture was then sonicated and stirred for 45 min each. Afterwards, the mixture was transferred into an autoclave and heated at 180 °C for 16 h in a Muffle furnace. The next day, the obtained product was washed multiple times with DIW and ethanol to remove residual impurities. The precipitates were collected and desiccated in an oven at 60 °C for several hours. Ultimately, the dried sample was calcined in a Nabertherm furnace at 550 °C for 3 h. At this stage, the core CCO material was ready for further testing and applications.

2.2 Synthesis of CCO/CNT composites

CCO/CNT composites with varying weight percentages of CNTs (3, 6, and 9%) were synthesized using the solvothermal method. The CCO phase and CNTs, in their respective proportions, were mixed in a beaker containing 50 mL of solvent. Ethanol was used as a solvent due to its superior dispersion properties and compatibility with oxides and many inorganic materials. The solution was then sonicated and stirred for 30 min each to ensure uniform dispersion and homogeneity. The homogeneous mixture was transferred into an autoclave and subjected to heat treatment at 180 °C for 3 h. After this physical reaction, the resulting solution was washed entirely to collect the precipitates, which were then dried in an oven at a low temperature.

2.3 Fabrication of electrodes

For electrode preparation, nickel foam (NF) (1 × 1 cm^2) was initially treated with dil. HCL to remove surface oxides and

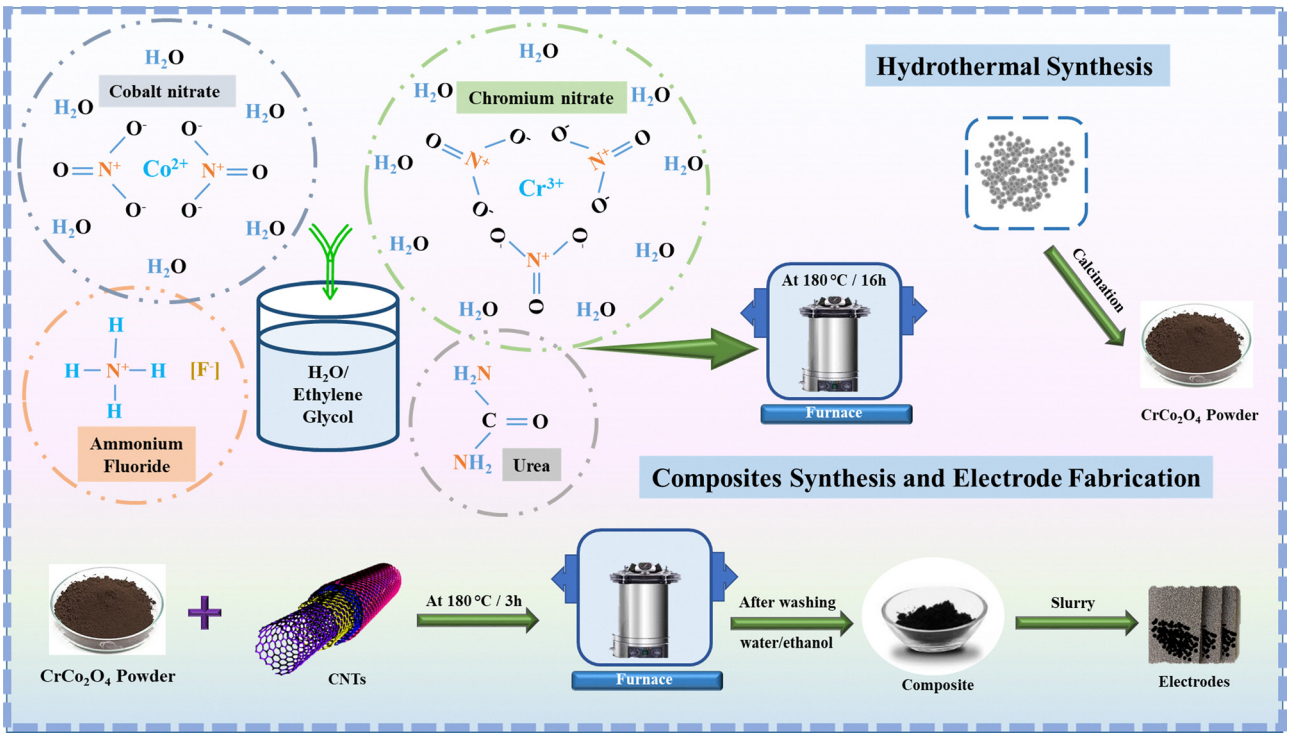

Fig. 1 Schematic representation of the synthesis process for CCO *via* a hydrothermal method and subsequent electrode fabrication of the CCO/CNT composites assisted by a solvothermal process.

impurities.[25] The foam was immersed in the acidic solution (1 : 3 acid to DIW), sonicated for 1 h, and then thoroughly washed with water. It was then subjected to a second sonication in DIW for an additional hour to ensure complete cleaning. Meanwhile, a slurry was prepared using matrix material, activated carbon (AC), and binder polyvinylidene fluoride (PVDF) in an 8.5 : 0.5 : 1 ratio, respectively. The binder was prepared using 300 mg of PVDF in a 15 mL dimethylformamide solution. The mixture was stirred for 8 h to achieve consistency. The final slurry was then deposited onto the cleaned Ni foam using a pipette. The electrode weights were carefully measured before and after deposition ($\pm$1 mg cm^{-2}), and the fabricated electrodes were subsequently used for EC testing. A schematic illustration of this whole synthesis process is depicted in Fig. 1.

3. Experimental

A combination of experimental techniques and theoretical modelling was employed to analyze the EC properties of the composites. The structural characteristics were examined through X-ray diffraction (XRD) carried out *via* a Shimadzu XRD-6100, which enabled precise phase identification and crystallographic analysis. The morphological attributes were analyzed with an ultra-fine resolution scanning electron microscope (Nano-Nova SEM-450) to assess minor structural features. Transmission electron microscopy (TEM, JEOL's Ltd) was employed to reveal the detail and microstructural properties of the particles. The elemental composition and distribution were estimated through energy-dispersive X-ray spectroscopy (EDS) utilizing an Oxford instrument, allowing for accurate elemental mapping. EC evaluations were carried out utilizing Corrtest electrochemical and corrosion studio (Version 6.4). A three-electrode assembly was utilized, comprising a counter electrode of Pt wire, a reference electrode (RE) of Ag/AgCl, and the respective working electrode (WE), all submerged in a 1 M KOH solution, utilized as an electrolyte. Cyclic voltammetry (CV), electrochemical impedance spectroscopy (EIS), the galvanostatic intermittent titration technique (GITT) and galvanostatic charge–discharge (GCD) tests were performed to investigate the material's EC behaviour. The EIS data were further analyzed to understand ionic conductivity and relaxation time, providing deeper insights into the material's performance. Asymmetric two-electrode testing was also conducted to evaluate the real-time EC performance for practical applications.

3.1 Crystallographic analysis

The structural characterization and the phase homogeneity of the as-synthesized samples deposited on NF were investigated using XRD analysis. Fig. 2(a) presents the XRD pattern of the materials recorded in the 2θ interval spanning from 20° to 80°. Well-defined and distinct diffraction peaks for NF were observed at 2θ = 18.8°, 30.9°, 36.5°, 44.6°, 58.7°, and 64.5°, corresponding to the (111), (220), (311), (400), (511), and (440) planes, respectively. These peaks are in good agreement with the ICSD reference ID number 00-024-0326, belonging to the $Fd\bar{3}m$ space group symmetry. These *hkl* values were utilized to calculate the lattice constant, which was determined to be 8.16 Å for the pure CCO.

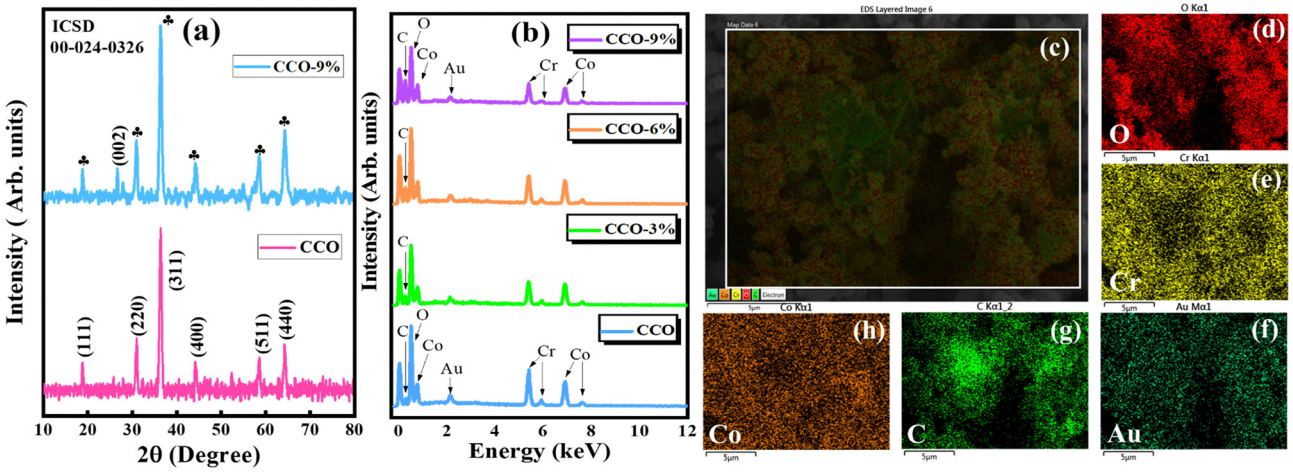

Fig. 2 (a) XRD spectra of CCO and CCO-9%, (b) EDX spectra of CCO, CCO-3%, CCO-6%, and CCO-9%, (c) a whole scanned surface, and (d)–(h) elemental mapping of all possible elements in CCO-9%.

No significant changes were observed in the XRD patterns after introducing varying concentrations of CNTs at 3, 6, and 9% into the CCO sample. The diffraction peaks of CCO remained unchanged in both position and intensity, suggesting that the incorporation of CNTs didn't alter the crystallinity or phase composition of the CCO material. An additional peak was also observed at $2\theta = 26.6^{\circ}$, attributed to the carbon content in the sample. The peak matched with the ICSD card number 00-026-1076, indicating the hexagonal crystal system in the CCO-9% composite. Moreover, the lattice constant was measured to be the same as for pure CCO. These results suggest that CNTs, even at concentrations of up to 9%, do not alter the crystallographic parameters of CCO, confirming the effective synthesis of these materials.[26]

3.2 Compositional analysis

The EDS spectra served as a powerful analytical tool to confirm elemental composition and assess material purity. Fig. 2(b) shows the EDS spectra of CCO and its composites CCO-3%, CCO-6% and CCO-9%. The spectra distinctly reveal the presence of Cr, Co, O and Au, validating the incorporation of CNTs into the CCO matrix. The elemental quantification aligns well with the expected stoichiometry, supporting the proposed interaction between the CCO and CNT phases in all composites. The characteristic peaks of all the elements along with the pronounced peak of C corresponds to the CNTs, providing insight into their dispersion and bonding with the matrix. The presence of Au peaks is attributed to the gold coating used in sample preparation, which enhances conductivity and improves FESEM imaging quality.[27] These findings affirm the well-controlled elemental composition and successful synthesis of the intended nanocomposites.

The composites were subjected to elemental mapping to probe the spatial distribution of the constituent elements. As shown in Fig. 2(c), a multicolored overlay represents different elements, confirming their uniform distribution throughout the composite structure. Additionally, Fig. 2(d)–(h) provides separate mapping profiles for Cr, Co, C, and O, each depicted in distinct colors. These maps substantiate the existence of each constituent and highlight their homogenous distribution. Regions with brighter colors correspond to elevated elemental concentration, whereas darker zones reflect diminished concentrations or a lack of specific elements.

3.3 Morphological features

Morphology is a critical parameter in determining the material's EC properties. EC performance strongly depends on the specific particle shape and its distribution.[28] The surface attributes of all the synthesized samples were examined through FESEM analysis at an ultra-high magnification of 100 000×. As depicted in Fig. 3(a), the CCO material primarily consists of well-defined spherical particles. The distinct morphology is particularly beneficial due to high volumetric E_d and low surface energy, which collectively enhance its functional efficiency in various applications.[29] Furthermore, the pure CCO material exhibits sufficient porosity, which can be seen in the inset of Fig. 3(a) at a resolution of 2 μm.

Upon introducing the CNTs into the CCO matrix, the particles develop a rough surface texture, as depicted in Fig. 3(b)–(d), which further increases the effective surface area, ultimately increasing the ion diffusion and electrical conductivity.[30] This geometrical transformation is likely attributed to the solvothermal interactions between CCO particles and CNTs, which facilitate surface modifications at the nanoscale. The integration of CNTs also modifies the surface features of CCO-3% and enhances surface porosity, ensuring a conductive channel within the composite. A similar trend was found for CCO-6% and CCO-9% where the surface features alter due to the integration of CNTs. In particular, CCO-9% exhibited larger particles as compared to other composite materials. The average particle size was found within the range of 200–300 nm, as depicted in Fig. 3(e)–(h). The distribution of CNTs over the composites can be seen in all samples, where CNTs form interconnected networks. Although this network maintains electrical conductivity, the excessive CNT content in some cases

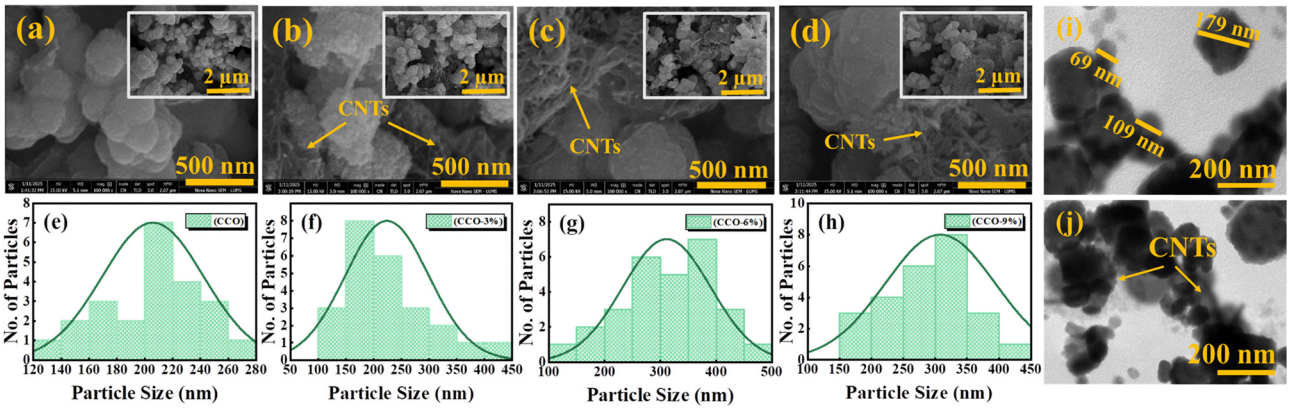

Fig. 3 (a)–(d) FESEM images of CCO, CCO-3%, CCO-6%, and CCO-9% at different magnifications, (e)–(h) along with their histograms of estimated particle size, and (i) and (j) TEM images of CCO and CCO-9%.

can reduce the mean free path, thereby restricting ion transport and potentially hindering the EC performance.[31] Even dispersion and uniform morphology throughout the samples depict the consistency and concordance, contributing to the enhanced EC features.

In addition, to clearly view the inner details and primary characteristics of the particles, TEM analysis was carried out for the CCO and CCO-9%, as given in Fig. 3(i) and (j). The pristine CCO material exhibited quasi-spherical and loosely aggregated particles with well-organized boundaries. The majority of particles lie within the nanometer range, while limited agglomeration leads to the formation of larger particles. These limited agglomerations, nanoscale boundaries, and well-defined particle distribution underscore the desired morphology for the CCO and CCO-9% composite. Moreover, the presence of CNTs in the CCO-9% exhibits a strong interfacial contact between the two matrices. This favorable morphology promotes more active sites and enhances the ion transportation during charging–discharging cycles, beneficial for enhancing the EC performance of the materials.

3.4 Voltammetric study

CV was utilized to analyze the underlying charge storage characteristics of the samples, providing valuable insight into their EC characteristics. The CV curves were recorded at various scans within a stable potential window (PW) of 0.0 to 0.5 V to analyze the charge storage behaviour and its characteristics. The oxidative and reductive peak responses detected across varying scan rates (SRs) correspond to reversible faradaic redox reactions, governing the charge storage mechanism. These redox transitions involve the EC conversion of the active material, as represented by the following reaction,

$$(CrCo_2O_4 + 4H_2O + 3e^-) \leftrightarrow (Cr^{3+} + 2Co^{2+} + 8OH^-)$$

This equation reveals critical insights about the electron transfer dynamics associated with the redox transitions in the 1 M KOH medium. The schematic illustration of the chemical reaction in a three-electrode study is depicted in Fig. 4(a). The oxidation state variations facilitate the transfer of three electrons, signifying the underlying redox mechanism. From these redox reactions, the theoretical capacity ($Q_{sp\text{-}theoretical}$) can be estimated, providing a criterion to correlate with the experimentally obtained capacitance values. The $Q_{sp\text{-}theoretical}$ is determined utilizing the following eqn (1).

$$Q_{sp\text{-}theoretical} = n \times (F/M_w) \quad (1)$$

Here, n represents the number of exchanged electrons, F denotes the Faraday constant (96 485 C mol^{-1}), and M_w corresponds to the molecular mass of CCO, with a value of 233.86 g mol^{-1}. Utilizing these parameters, the $Q_{sp\text{-}theoretical}$ is computed to be 1237.77 C g^{-1}. Furthermore, the incorporation of CNTs can significantly enhance the EC activity, leading to an improvement in the overall energy storage response of the system.

Fig. 4(b)–(e) presents the voltammograms of CCO and its composites at SRs of 1–50 mV s^{-1}. The observed redox peaks indicate that the primary charge storage mechanism is governed by the hybrid behaviour, involving the faradaic and non-faradaic charge storage processes. The consistent symmetry of the peaks across different SRs suggests excellent cycling stability and reversibility. A slight shift in the CV curves towards higher and lower potentials during the anodic and cathodic sweeps, respectively, is associated with polarization effects.[32] Additionally, it indicates the influence of electrode resistance and ion diffusion-controlled charge storage processes. Each voltammogram exhibits a non-rectangular shape with distinct redox peaks, providing further evidence that the charge storage process is dominated by pseudocapacitive behavior. The improved ionic and charge transport kinetics at elevated potentials result from rapid and reversible faradaic processes localized at the electrode–electrolyte (E/E) interface. These EC processes enable efficient electron transfer and ion diffusion, thereby enhancing the current response and significantly increasing the charge storage capacity compared to the conventional non-faradaic mechanisms. Additionally, the increased area of the CV loop signifies an improvement in ionic intercalation

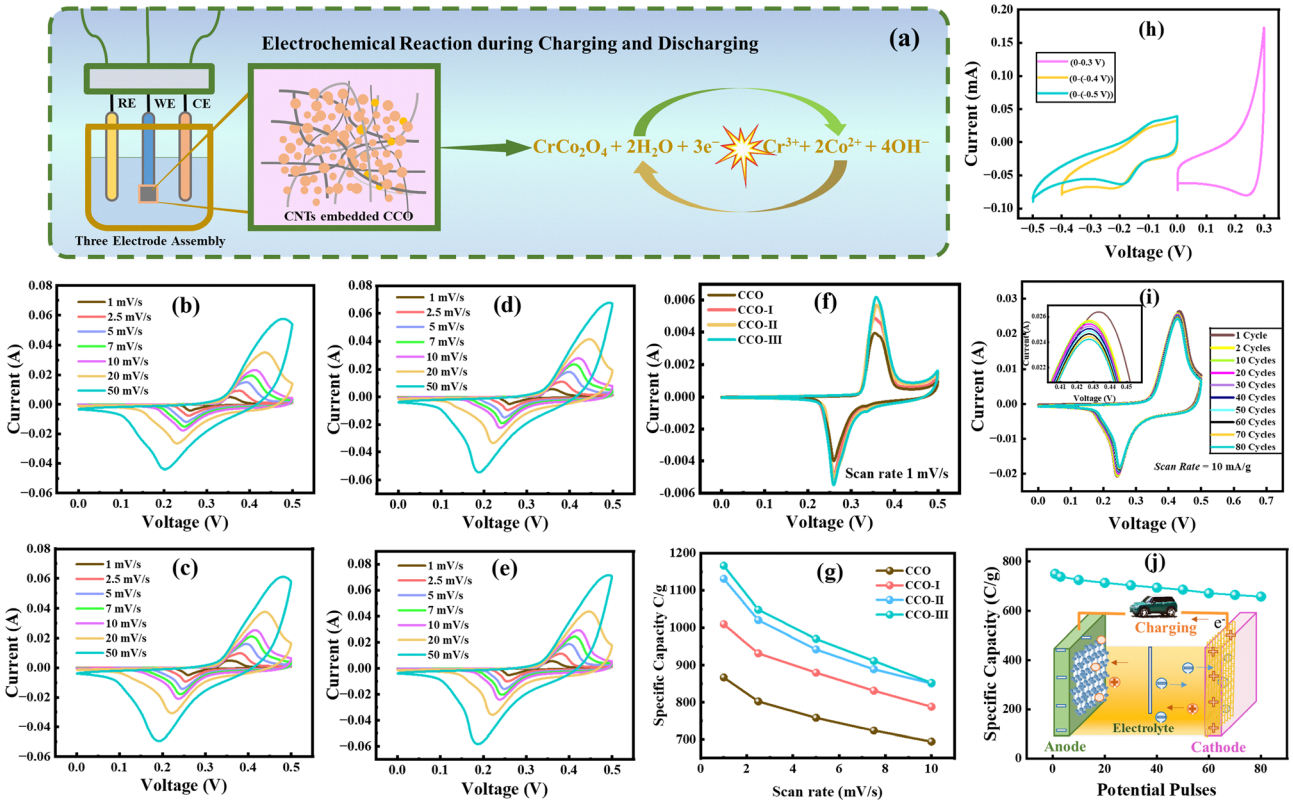

Fig. 4 (a) Schematic illustration of the EC process during charging and discharging, (b)–(e) CV curves at different scan rates for (a) CCO, (b) CCO-3%, (c) CCO-6%, and (d) CCO-9%, (f) comparison of the CV curves of all samples at a scan rate of 1 mV s^{-1}, (g) variations of scan rate *vs.* specific capacity, (h) CV curves in the negative potential window (−0.4 to 0 V) and in potential window (0–0.5 V) for CCO-9%, (i) CV curves for CCO-9% across different cycles at a scan rate of 5 mV s^{-1}, and (i) variation of potential pulses *vs.* specific capacity.

sites, thereby enhancing the overall EC performance, as given in Fig. 4(f).[33]

The integration of CNTs in the SC electrodes offers several advantages, including high electrical conductivity, superior stability, a large specific surface area and enhanced EC performance. The Q_{sp} for each composition is determined using eqn (2).

$$Q_{sp} = \int_{V_a}^{V_c} I(V)\mathrm{d}V/(m \times v) \quad (2)$$

The equation incorporates several key parameters, including the active material's mass (m), the applied SR (v), and the integrated current across the potential window, which corresponds to the integrated area beneath the CV curve. For CCO, the highest Q_{sc} was recorded as approximately 1009 C g^{-1} at the SR of 1 mV s^{-1}. However, this value reduces gradually with increasing SRs, mainly attributed to limited ion diffusion in the electrolyte at higher SR.[34] A noticeable reduction in Q_{sc} is observed, decreasing from 1009 to 931, 879, 831, 788, 652 and 406 C g^{-1}.

Based on the results, incorporating hybrid composites into SC systems is a promising strategy for improving their EC performance.[35] The addition of CNTs notably enhanced both the anodic and cathodic peak currents, indicating more efficient and rapid ion transport during redox processes. The composite electrodes CCO-3%, CCO-6% and CCO-9% display prominent redox peaks across the potential interval of 0–0.5 V. With increasing SRs, these peaks shift toward the positive and negative extremes of the potential window. At a SR of 1 mV s^{-1}, the Q_{sc} values for CCO-3%, CCO-6% and CCO-9% are 1009, 1130 and 1165 C g^{-1}, respectively. A detailed summary of these values across various SRs is presented in Table 1 as well as depicted in Fig. 4(g). Furthermore, the significant improvement in capacity is directly linked to the presence of CNTs in the composites.

3.4.1 Impact of negative potential and cycling on the CV loop behaviour. Applying negative bias to the WE enables a thorough examination of its structural and EC properties. Within this setup, the WE is polarized negatively relative to

Table 1 Specific capacity from CV analysis of CCO and its composites at different scan rates

Scan rates (mV s^{-1})	CCO (C g^{-1})	CCO-3% (C g^{-1})	CCO-6% (C g^{-1})	CCO-9% (C g^{-1})
1	866.73	1009.54	1130.79	1165.91
2.5	802.39	931.53	1020.43	1048.32
5	758.24	879.76	942.13	970.34
7.5	723.72	831.37	888.90	911.23
10	694.39	788.01	850.55	852.50
20	598.25	652.48	730.45	700.19
50	385.55	406.02	447.24	418.67

the RE. This negative bias influences the surface characteristics and interfacial charge interactions, making it possible for assessment of the energetic demands for species adsorption or their reduction in the electrolyte medium.[36,37] The potential of zero charge (PZC) refers to the specific condition where the surface of the electrode carries no net charge. This condition encourages the accumulation of cationic species, such as K^+, originating from the electrolyte medium.[38]

For this, CV was conducted with the different potential ranges of 0 to −0.4 V and −0.5 V, to study the EC behaviour of the electrode as shown in Fig. 4(h). The CV curves in both loops exhibited well-defined profiles, indicating faradaic behaviour.[39] As the applied potential was increased to −0.5 V, a small increment in current was observed, suggesting a higher storage capacity. This indicates that the electrode material remains electrochemically stable even under more negative polarization conditions, affirming the material's suitability for SC applications.

The CV profile is governed by the unique properties of the electrode material and the electrolyte-driven EC processes. First, CV cycling promotes surface optimization and ion intercalation, leading to system stabilization. As the number of cycles increases, the loop's surface area expands considerably, which enhances ion dynamics and activates the surface, thus improving the ion transport kinetics and electrode accessibility.[40,41] The CV curves of the CCO, measured over 80 consecutive cycles, exhibit a stable loop with minimal fluctuations in peak current (I_p), as shown in Fig. 4(i). Although no shift in peak potential occurred with the number of cycles, a progressive decline in the I_p was observed, indicating the anticipated deterioration of the electrode material with continuous cycling.[42] The variation of Q_{sc} with respect to cycle number is shown in Fig. 4(j).

3.4.2 Theoretical evaluation performed *via* Dunn's model. To assess the charge storage performance of the material and its charge storage mechanism, the Dunn model was employed. This model enables a quantitative evaluation of the contributions from capacitive and diffusion-governed storage mechanisms.[43] By analyzing CV voltammograms recorded at varying SRs, the relative contributions of these mechanisms were determined. A comparative analysis helps to distinguish whether the charge storage mechanism is predominantly capacitive, or indicative of pseudocapacitive behavior, especially at higher SRs. This approach provides a systematic methodology for differentiating between capacitive and diffusive charge storage processes.[44] To further examine the charge storage characteristics, Cottrell's equation was utilized as given in eqn (3).

$$I_p = a(v)^b \quad (3)$$

In this equation, v represents the SR, while I_p denotes the peak current, and a and b represent tunable parameters. Among these, the value of b is the most critical factor, as it determines the predominant charge storage mechanism. The correlation between $\log(I_p)$ and $\log(v)$ provides insight into the charge storage behavior, where the slope obtained from the $\log(I_p)$ *vs.* $\log(v)$ plot corresponds to the b-value. If $b = 0.5$, the mechanism is diffusive-controlled, indicating a faradaic charge accumulation mechanism. If $b = 1$, the mechanism is purely capacitive, signifying a non-faradaic charge storage mechanism. However, if b falls between 0.5 and 1, the system exhibits a hybrid charge storage behavior, integrating both capacitive and diffusion-controlled contributions.[45,46] To further quantify these contributions, eqn (3) was modified to distinguish between capacitive and diffusive charge storage mechanisms, given as below,

$$i(v) = i_{capacitive}(v) + i_{diffusive}(v) \quad (4)$$

Thus, the total current can be represented as:

$$i(v) = k_1(v) + k_2(v^{1/2}) \quad (5)$$

Here, $i(v)$ represents the peak current, k_1 corresponds to the slope and k_2 denotes the intercept. By plotting $i/v^{0.5}$ on the vertical axis against $v^{0.5}$ on the horizontal axis, the value of k_1 and k_2 can be quantified.[47] The capacitive and diffusive contributions are calculated governing the equation given below.

$$\text{Capacitive contribution } (\%) = \frac{i(\text{capacitive})}{i(\text{capacitive}) + i(\text{diffusive})} \times 100 \quad (6)$$

The diffusion contribution (%) can be calculated by subtracting the value of the capacitive contribution from 100. For pure CCO, the b-values were determined to be 0.78 and 0.76 for the anodic and cathodic peak currents, respectively, with an average value of 0.77. The corresponding k_1 and k_2 values were 0.00139 and 0.00296, respectively. Based on these parameters, the capacitive and diffusive charge storage contributions were calculated to be 43% and 57%, respectively. Upon incorporating CNTs as in CCO-3%, the b-values decreased to 0.64 and 0.74, with an average of 0.71, while the k-values were $k_1 = 0.0012$ and $k_2 = 0.0043$. This composition delivered 31% and 69% of capacitive and diffusive contributions, respectively. For CCO-6%, the average b-value was 0.72, with corresponding $k_1 = 0.0007$ and $k_2 = 0.0033$, leading to capacitive and diffusive charge storage contributions of 25% and 75%, respectively. In the case of CCO-9% incorporation, the average b-value further decreased to 0.66, while the k_1 and k_2 values were 0.00073 and 0.00482, respectively. This composition exhibited the lowest capacitive contribution (19%) and the highest diffusive contribution (81%). The b-values and their proportional contributions in all the samples are given in Fig. 5(a)–(l).

The analysis of the charge storage contribution indicates that CCO-based materials, especially CCO-9% are well-suited for hybrid SC applications. However, contrary to the expected trend, the incorporation of CNTs led to an increased reliance on diffusion-controlled charge storage while reducing the capacitive contribution. The observed decline in b-value, from 0.77 (pure CCO) to 0.66 (9% CNTs), signifies a transition toward a more diffusion-dominated charge storage mechanism. Consequently, the diffusive contribution increased from 58% to 80%, while the capacitive contribution declined from 42%

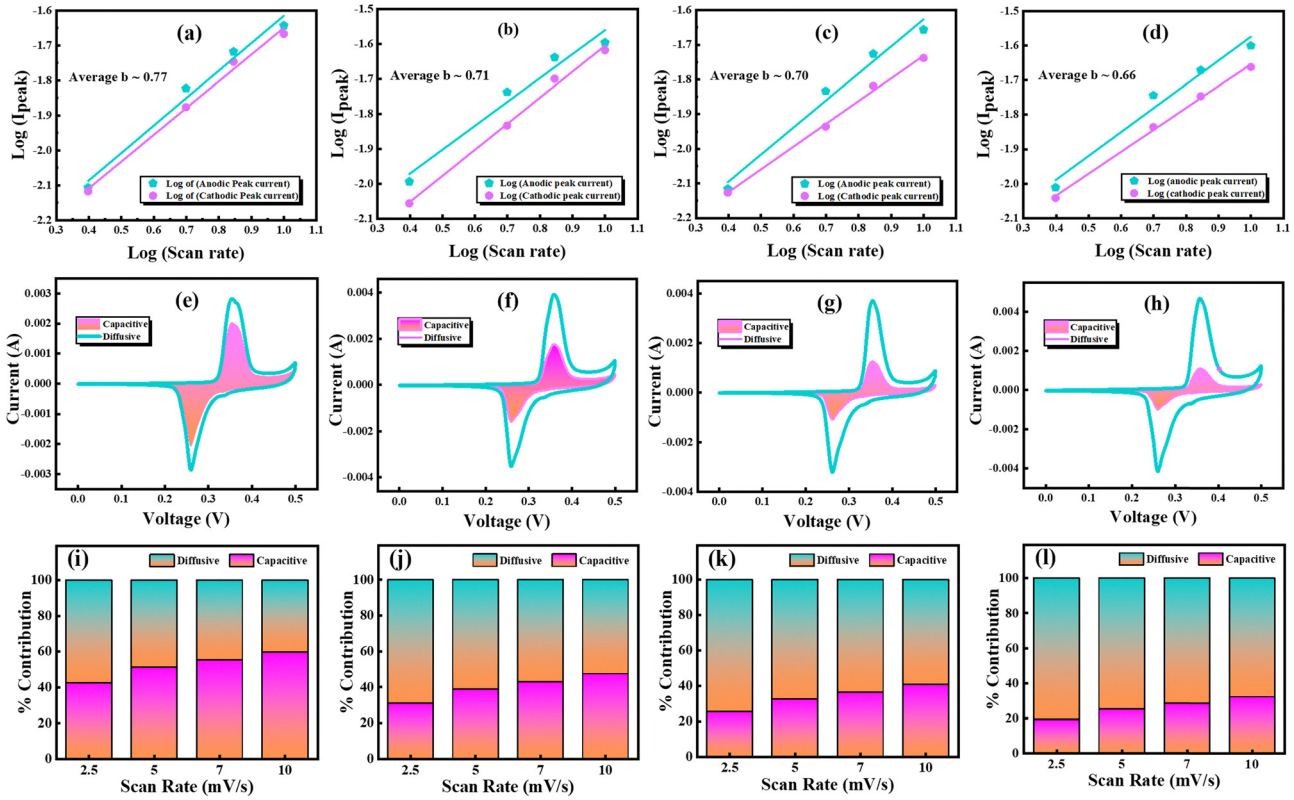

Fig. 5 (a)–(d) Power law's plot for CCO, (b) CCO-3%, (c) CCO-6% and (d) CCO-9%, (e)–(h), CV profiles recorded at the lowest scan rate 1 mV s^{-1} showing percentages of capacitive and diffusive current contribution, and (i)–(l) percentage graph of diffusive and capacitive currents attained from the Dunn's plots for all the samples at different scan rates.

(pure CCO) to 20% (9% CNTs). A contributing factor may be that the incorporation of CNTs into the CCO matrix increases the available surface area for redox reactions, thereby enhancing diffusion pathways. However, since the CNT content is relatively low compared to CCO, the charge storage remains predominantly PC-dominated, with only a minor contribution from EDLC. Moreover, previous studies align with these findings, indicating that the incorporation of carbon-based materials can impede electrolyte accessibility, thereby restricting capacitive charge storage.[48] Furthermore, investigation on the metal oxide/CNT composite suggests that structural disruption and poor CNT dispersion at higher concentration negatively impact the effective capacitance, further contributing to the shift toward diffusion-controlled charge storage behavior.

3.5 Galvanostatic charge–discharge analysis

GCD testing is a crucial EC technique for evaluating the performance of ESDs, including SCs and batteries. Fig. 6(a)–(d) presents the GCD profiles of CCO and its composites, recorded at J ranging from 1.3 to 8.4 A g^{-1}. Each graph illustrates the charging and discharging cycles corresponding to the voltage response over time. The nearly symmetrical nature of the curves indicates excellent EC reversibility, rate capability and stability. With increasing J, a reduction in discharge time was observed, primarily due to the limited ion diffusion within the E/E interface.[49,50] The Q_{sp} is observed with increasing J for all compositions, primarily due to the reduced ion diffusion time at higher currents. Non-linear graphs also validate the hybrid nature of the electrodes. The charge storage capacities (Q_{sp}) of all the electrodes were evaluated at various J utilizing eqn (7).

$$Q_{sp} = I \times (\Delta t/m) \quad (7)$$

where I corresponds to the applied current, m represents the mass of electrode material, and Δt is the discharge time. Spinel CCO exhibited remarkable charge–discharge characteristics. For CCO, a charge–discharge time of 378.4 s was recorded at the J of 1.3 A g^{-1}, highlighting the dominance of faradaic redox processes and confirming its high Q_{sp} of 513.20 C g^{-1}. Furthermore, the pristine CCO achieved an E_d of 35.63 Wh kg^{-1} and a P_d of 338.98 W kg^{-1}, as determined using eqn (8) and (9).

$$E_d = Q_{sp} \times \Delta V/(2 \times 3.6) \quad (8)$$

$$P_d = (E_d \times 3600)/\Delta t \quad (9)$$

The calculated EC parameters are presented in Table 2. Literature reports consistently highlight that binary metal oxides outperform their single metal counterparts in terms of charge storage efficiency, thereby enhancing overall device performance.[51,52] The maximum discharge durations were observed to be 439.06, 521.04, and 602.75 s for CCO-3%, CCO-6% and CCO-9%, respectively, as shown in Fig. 6(e). These prolonged durations indicate improved

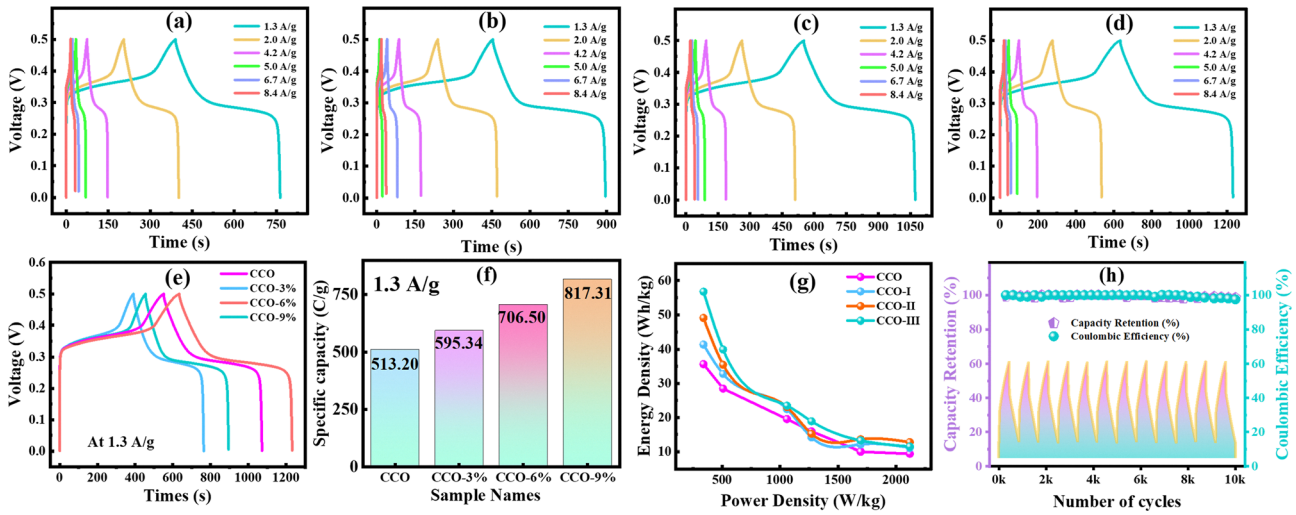

Fig. 6 (a)–(d) GCD curves at different currents for CCO, CCO-3%, CCO-6%, and CCO-9%, (e) comparison of the GCD curve at 3.3 A g^{-1} current, (f) variation of specific capacity sample to sample, (g) interplay between power density *vs.* energy density, and (h) cycling stability of CCO-9%.

Table 2 Variation of specific capacity and energy density with power density for the CCO, CCO-3%, CCO-6%, and CCO-9% composites from GCD analysis

Sample	Current density (A g^{-1})	Discharge time (s)	Specific capacity (C g^{-1})	Energy density (Wh kg^{-1})	Power density (W kg^{-1})
CCO	1.35	378.4	513.20	35.63	338.98
	2.03	201.6	410.11	28.48	508.47
	4.23	73.2	310.31	21.54	1059.32
	5.08	45.1	229.38	15.92	1271.18
	6.77	21.3	144.52	10.03	1694.91
	8.47	16.0	136.02	9.44	2118.64
CCO-3%	1.35	439.26	595.34	41.34	338.98
	2.03	232.05	471.99	32.77	508.47
	4.23	86.54	366.71	25.46	1059.32
	5.08	40.13	204.04	14.16	1271.18
	6.77	25.73	174.44	12.11	1694.91
	8.47	18.95	160.60	11.15	2118.64
CCO-6%	1.35	521.35	706.50	49.06	338.98
	2.03	251.04	510.60	35.45	508.47
	4.23	92.03	389.96	27.08	1059.32
	5.08	43.12	219.28	15.22	1271.18
	6.77	29.19	195.92	13.60	1694.91
	8.47	21.63	183.36	12.73	2118.64
CCO-9%	1.35	602.34	817.30	56.75	338.98
	2.03	270.76	550.69	38.24	508.47
	4.23	95.73	405.66	28.17	1059.32
	5.08	45.05	229.07	15.90	1271.18
	6.77	28.51	190.90	13.25	1694.91
	8.47	19.85	168.29	11.68	2118.64

reaction dynamics. A significant enlargement in the values of both E_d and P_d was also evident. The Q_{sp} values determined for CCO-3%, CCO-6%, and CCO-9% of 595.34, 706.50 and 817.30 C g^{-1}, respectively, are given in Fig. 6(f). CCO-3% exhibited an E_d of 41.34 Wh kg^{-1} with a corresponding P_d of 338.98 W kg^{-1}. A continuous increment was observed in the value of E_d for CCO-6% and CCO-9% as 49.06 and 56.75 Wh kg^{-1}, respectively. The Ragone plot depicted in Fig. 6(g) offers a comprehensive visualization of the trade-off between E_d and P_d among the prepared samples. Moreover, the interplay between these values with SRs is presented in Table 4. These results highlight the suitability of the composites for hybrid energy system applications.

In addition, the cycling stability of CCO-9% was evaluated at a J of 0.3 A g^{-1} over 10 000 cycles. The electrode demonstrated excellent stability, maintaining 98% of its original capacity along with 97% coulombic efficiency, as shown in Fig. 6(h). These outcomes showcase the strong potential of the synthesized composite as an effective electrode sample for SCs.

3.6 Galvanostatic intermittent titration technique

The GITT is an EC technique utilized to evaluate the diffusion coefficient of the materials.[53] During GITT analysis, the electrode material is subjected to a series of current pulses. In this study, a charging current of 1 mA was applied for a specified

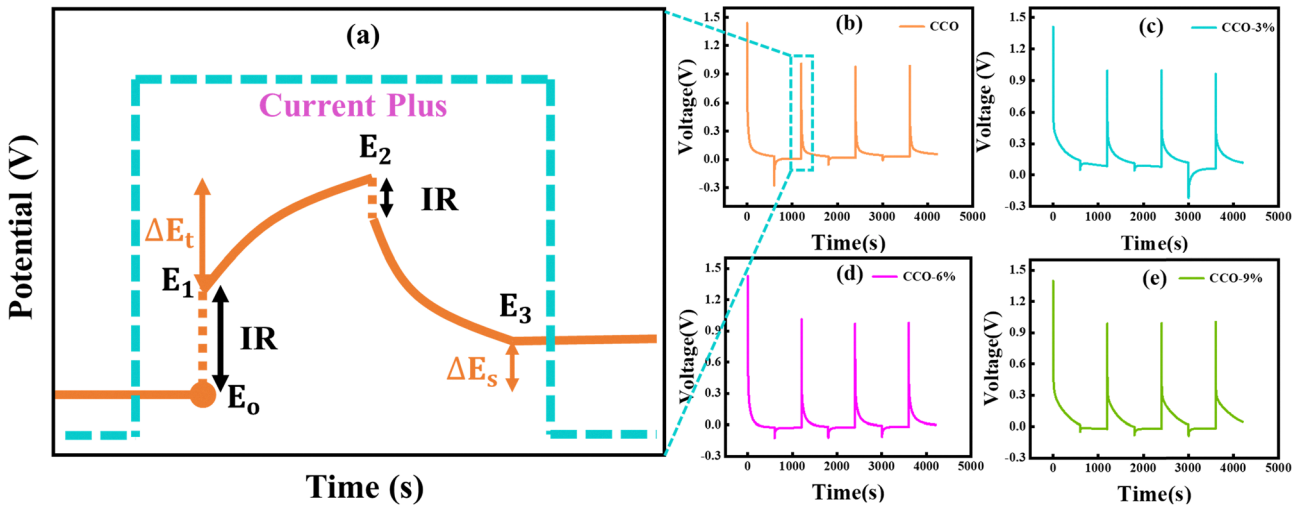

Fig. 7 (a) Schematic illustration of a single GITT plot, (b)–(e) GITT profiles of the CCO, CCO-3%, CCO-6%, and CCO-9% electrodes, showcasing the voltage response during intermittent current pulses.

duration. Each applied current pulse was accompanied by a subsequent relaxation stage during which no current was applied, allowing the system to approach a quasi-equilibrium state. GITT-based EC measurements were carried out within the voltage range spanning 0 to 0.4 V. The GITT profiles depicted in Fig. 7(a) exhibit an instantaneous potential jump to the applied constant current, corresponding to the Ohmic IR drop, offered by the electrolyte, WE and constant resistances. This IR drop ($E_o - E_1$) was extracted from the calculations, and the transient response was calculated as $\Delta E_t = E_2 - E_1$, where E_2 represents the WE potential after the small constant current pulse, and E_1 corresponds to the immediate potential just applying the constant current pulse (after a sharp IR drop). The steady-state change was calculated from the relaxation portion $\Delta E_s = E_3 - E_0$, where E_3 is the potential after the relaxation time period (and starting point for the next cycle), and E_0 represents the initial equilibrium of WE potential. The average time interval of each step in this process was approximately 10 min. The diffusion coefficient measured by using the formula is provided below in eqn (10).

$$D = \frac{4}{\pi\tau}\left(\frac{m_B V_m}{M_B S}\right)^2 \left(\frac{\Delta E_s}{\Delta E_t}\right)^2 \quad (10)$$

In the given formula, m_B represents the active material mass used in the electrode, while M_B denotes its molar mass. Moreover, V_m corresponds to the molar volume of CCO, S signifies the electrode's surface area and τ represents the duration of the current. ΔE_s and ΔE_t are directly calculated from the graph given in Fig. 7(b)–(e). According to the analysis, the diffusion coefficient of pure CCO was found to be approximately 2.35×10^{-11} cm^2 s^{-1}. Higher diffusion coefficients are associated with enhanced rate capability and long-term cycling durability.

The hybrid electrodes CCO-3%, CCO-6% and CCO-9% incorporating CNTs exhibited significantly improved diffusion coefficients of value 2.09×10^{-10}, 2.34×10^{-10}, and 2.65×10^{-10} cm^2 s^{-1}, respectively. CCO-9% exhibited a high diffusion coefficient among all the composites, which is attributed to the presence of CNTs.[54,55] Additionally, CNTs effectively reduce the interfacial resistance, thereby improving the overall electrical conductivity and efficient ion transport channels at the E/E interface. Moreover, the increased porosity, which is attributed to the presence of CNTs, also promotes faster and easier electron flow. These factors collectively enhance the diffusion dynamics, highlighting CCO-9% as a strong candidate for SC applications.

3.7 Electrochemical impedance spectroscopy

EIS was carried out to analyze the intrinsic reaction kinetics, ion diffusion and charge transfer mechanisms of the newly synthesized CCO and its composites over a frequency range of 0.01 to 10^5 Hz. The respective Nyquist plots, along with the fitted equivalent circuit derived from the measured EIS data, are depicted in Fig. 8(a)–(d). These plots illustrate the relationship between the real component of impedance (Z') and the imaginary component of impedance (Z''), plotted on the horizontal axis and the vertical axis, respectively. This analysis provides valuable insights into key EC parameters, including charge transfer resistance (R_{ct}), solution resistance (R_s), capacitive behavior, and ion diffusion properties within the electrode material.[56,57]

In the Nyquist plot of pure CCO, the R_s is measured at approximately 1.32 Ω, accompanied by a pronounced semicircle, indicating relatively low conductivity. This suggests that pure CCO exhibits poor charge transfer capability at the E/E interface. With the incorporation of CNTs at low concentration in CCO-3%, R_s decreases slightly to ~1.26 Ω, while the semicircle is marginally reduced, signifying a moderate enhancement in conductivity. This improvement is likely due to the effective dispersion of CNTs, which optimizes electrical conductivity. At a moderate CNT concentration, CCO-6%, both R_s and the diameter of the semicircle decrease further, indicating a lower R_{ct} (7.69 Ω) compared to CCO-3%. At this concentration,

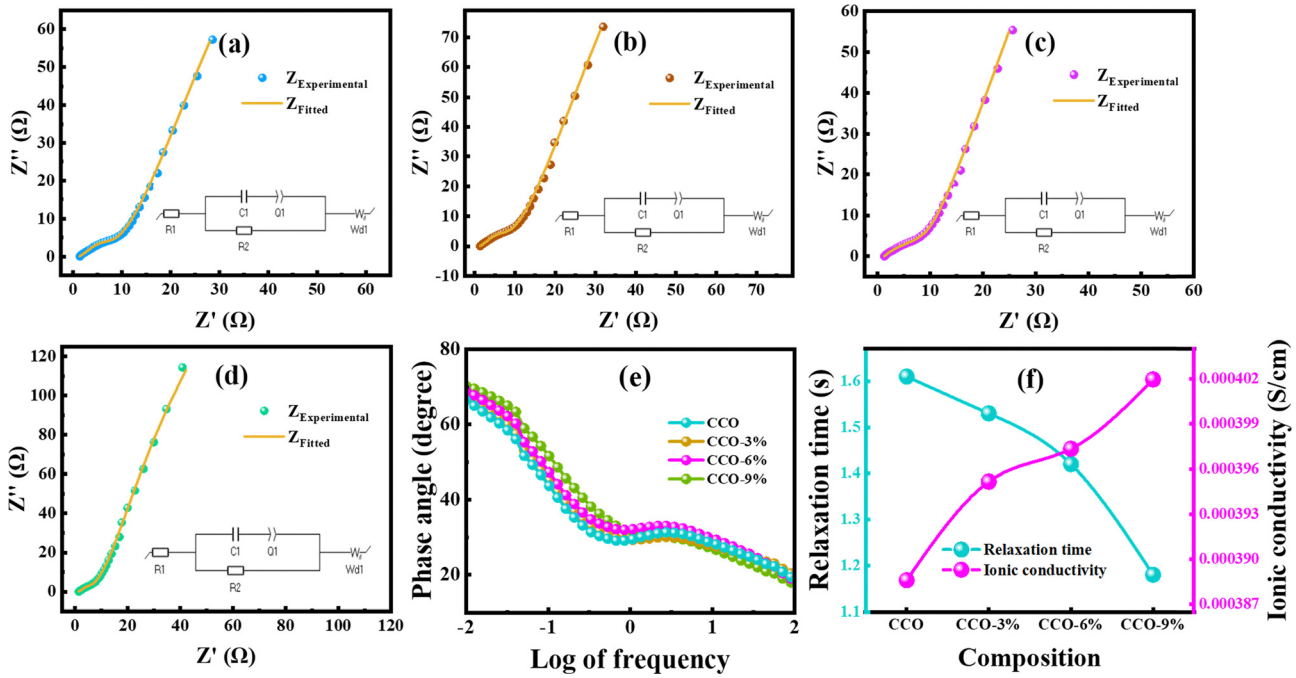

Fig. 8 (a)–(d) Nyquist plots of CCO, CCO-3%, CCO-6%, and CCO-9% nanomaterials, (e) Bode plots of novel materials, and (f) variation of ionic conductivity and relaxation time.

CNT dispersion remains effective, facilitating improved electron mobility and reducing charge transfer resistance. For CCO-9%, which contains the highest CNT concentration, the semicircle is significantly minimized, and R_s reaches its most favorable value of 1.24 Ω. This notable reduction in R_s is attributed to the increased CNT content, which enhances the charge transfer efficiency and overall conductivity.

At low frequencies, the Nyquist plots exhibit linear segments, which correspond to Warburg impedance (W_r), indicative of ion diffusion within the electrolyte solution. In particular, the CCO-9% demonstrates a pronounced reduction in slope within its linear region, suggesting significantly enhanced ion transport properties. This further confirms that CNT incorporation substantially improves the EC response, especially in CCO-9%, facilitating efficient ionic diffusion and charge transfer efficiency within the electrode material. The corresponding values are presented in Table 3.

3.7.1 Relaxation time. Discharge dynamics are assessed using the relaxation time constant (τ), another essential parameter in SC performance evaluation. This parameter represents the minimum time necessary for a SC to fully discharge, primarily manifested in the high-frequency region associated with resistive behavior. In contrast, in the lower frequency region, the system demonstrates resistive behavior.[58] The SC demonstrates ideal capacitive behavior at lower frequencies with minimal energy dissipation, as shown in Fig. 8(e). The coexistence of resistive and capacitive impedance within a particular frequency region defines the resonance frequency, subsequently utilized in the given equation to determine the (τ),

$$\tau = 1/(2\pi f_0) \quad (11)$$

The values of τ for CCO, CCO-3%, CCO-6% and CCO-9% were measured as 1.61, 1.53, 1.42, and 1.18 s, respectively. The minimum value of τ, indicative of an efficient charge transport behavior and enhancement in efficiency of electron and ion transfer during charge–discharge cycles, makes it highly suitable for applications demanding fast energy release.

3.7.2 Ionic conductivity. Being a crucial parameter, ionic conductivity of the electrolyte species is of pivotal importance in evaluating charge transfer efficiency during redox reactions and significantly impacts P_d by influencing the electrolyte's resistance. Higher ionic conductivity minimizes energy losses, ensuring a stable concentration gradient necessary for optimal SC performance.[59] It can be determined using the equation,

$$\sigma = \frac{L}{(R_i \times A)} \quad (12)$$

where L represents the electrode thickness, R_i and A correspond to the R_s and electrode surface area, respectively. The determined ionic conductivity values for all the electrode setups, presented in Table 4, indicate that CCO-9% exhibits the maximum value of conductivity, about 4.0×10^{-4} S cm^{-1}, signifying the minimal ion transport resistance and superior

Table 3 Values of elements for the corresponding fitted circuit, R_1 = R_s, R_2 = R_{ct}, Q_2 = constant phase elements, and W = Warburg impedance

Sample	R_1 (Ω)	R_2 (Ω)	Q_2 (F s$^{(a-1)}$)	W (Ω)
CCO	1.32	9.73	0.103	4.08
CCO-3%	1.26	8.33	0.106	2.06
CCO-6%	1.27	8.66	0.112	3.79
CCO-9%	1.24	7.69	0.312	0.86

Table 4 Calculated values of relaxation time, ionic conductivity and diffusion coefficient

Sample	Frequency (Hz)	Relaxation time (s)	Conductivity (S cm^{-1})	Diffusion coefficient (cm^2 s^{-1})
CCO	1.72	1.61	3.88×10^{-4}	2.35×10^{-11}
CCO-3%	1.74	1.53	3.95×10^{-4}	2.09×10^{-10}
CCO-6%	1.64	1.42	3.97×10^{-4}	2.34×10^{-10}
CCO-9%	1.79	1.18	4.02×10^{-4}	2.65×10^{-10}

conductivity across all the remaining samples. The variation in ionic conductivity across different compositions is depicted in Fig. 8(f). The charge delivery properties and enhanced ionic conductivity of CCO-9% position it as a promising material choice for smart energy gadgets that demand fast and efficient performance.

3.8 Asymmetric device configuration

To evaluate the real-time performance of CCO-9%, a two-electrode asymmetric device comprising CCO-9% as the cathodic electrode and AC as the anodic electrode in 1 M KOH electrolyte was tested. This method offers a practical and comprehensive evaluation of device-level EC performance as depicted in Fig. 9(a). For charge neutrality and to achieve optimized EC performance, the charge balance between the two electrodes was systematically maintained using the mathematical relation $m^+C^+V^+ = m^-C^-V^-$, where m, C, and V represent the electrode mass, specific capacitance, and operational potential window, respectively. Based on this criterion, the corresponding mass ratios were precisely calculated using eqn (13), thereby enabling balanced charge storage and maximizing energy retention.[73]

$$\frac{m^+}{m^-} = \frac{C^-\Delta V^-}{C^+\Delta V^+} \tag{13}$$

Additionally, alkaline KOH was chosen as the electrolyte owing to its wide EC stability window in aqueous media, low viscosity, and high ionic conductivity. The abundant OH^- ions in KOH promote rapid charge compensation during faradaic redox reactions, thereby accelerating electrode kinetics and minimizing internal resistance. In EC analysis, materials in a three-electrode system show better performance due to the controlled environment, likely due to the reference electrode, which leads to minimal internal resistance. On the other hand, two electrodes mimic the real-time values of EC features within the electrolyte. This led to more resistance, which decreases the EC performance of the cell.[60,61] The asymmetric response of CCO-9% underscores the battery-type charge storage mechanism of the composite.

To examine the potential-dependent features, the PW was extended up to 1.2 V. The CV curves shown in Fig. 9(b) and (c) show varying applied PWs. Almost the same shape of the CV curves was seen with the extended loop area. The synergistic effect due to both electrodes with the balanced mass proportion facilitated the expansion of the total cell voltage.[62,63] The broadened voltage improves the E_d as it is directly related to the square of the operating voltage, as discussed in Section 3.5.

The extended PW is attributed to the corresponding EC features of CCO-9%. The carbon electrodes and CNTs exhibit EDLC-type capacitance across a broad potential range, while CCO delivers a faradaic charge storage mechanism. The rectangular CV curve was observed within this potential range. It usually happens due to the asymmetric device design, as AC has EDLC behaviour, and in this two-electrode system, both electrodes participate in the EC reaction and offer high resistance. Moreover, potential drop and charge balancing across the entire cell suppress the redox features. Consequently, the CV curves appear more rectangular even if the material is battery-type. Another interesting feature was also observed, that CCO-

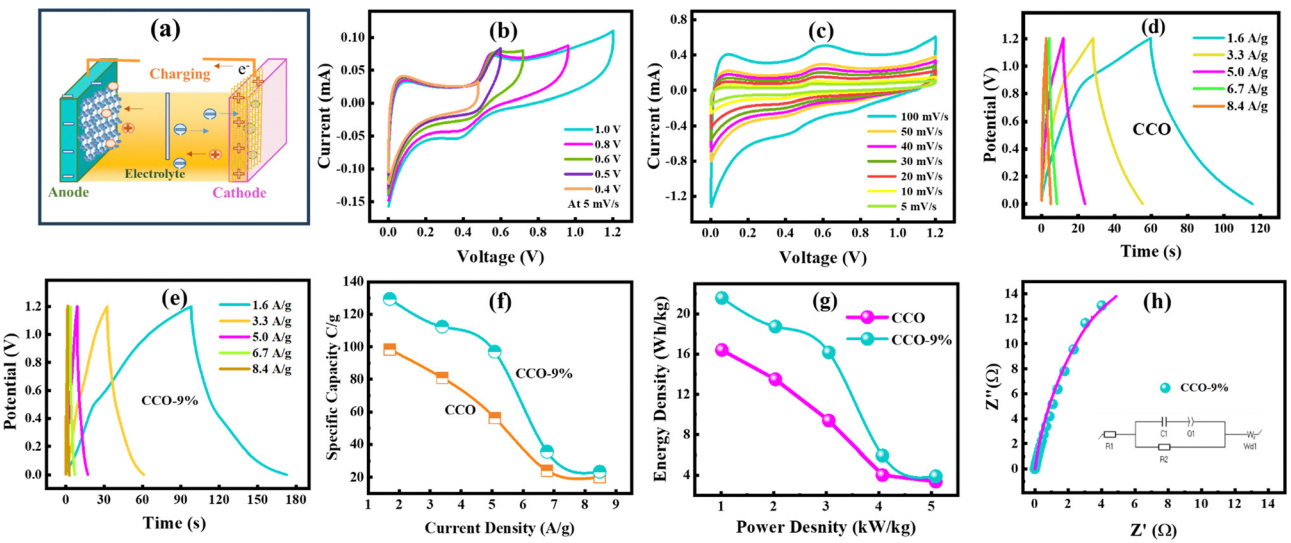

Fig. 9 (a) The mechanism of electrode testing, (b) and (c) CV plots of CCO-9% at various potential windows and scan rates, (d) and (e) GCD profiles of CCO and CCO-9% at different current densities, (f) variation of specific capacity with current density, (g) interplay of energy density and power density, and (h) Nyquist plot of the composite in a two-electrode configuration.

Table 5 A literature-based comprehensive table detailing the composition, synthesis routes, and electrochemical performance parameters of analogous materials for energy storage applications

Composition	Method	Q_{sp}, P_d, E_d	Diffusion coefficient ($cm^2\ s^{-1}$)	Cycling stability (%)	Ref.
$NiCo_2O_4$/CNTs	Chemical deposition	828 F g^{-1}, 0.7 KW kg^{-1}, 28.58 Wh kg^{-1}	N/A	99% (3k) cycle	68
$Mn_{0.06}Co_{2.94}O_4$/rGO	Hydrothermal	933 F g^{-1} (4 A g^{-1}), 9 KW kg^{-1}, 33 Wh kg^{-1}	N/A	82% (33k) cycle	69
$NiCo_2O_4$/CNTs	Hydrothermal	873 F cm^{-3} (0.5 A g^{-1}), 0.55 KW kg^{-1}, 27.6 Wh kg^{-1}	N/A	95% (5k) cycle	70
$CrCo_2O_4$/Co-MOF	Hydrothermal	1075 C g^{-1} (1.5 A g^{-1}), 1652 W kg^{-1}, 38 Wh kg^{-1}	N/A	90% (6k) cycle	71
$MnCo_2O_4$/rGO	Hummers' method	808 F g^{-1} (3 mV s^{-1}), 7658 W kg^{-1}, 15.2 Wh kg^{-1}	N/A	135% (1k) cycle	72
$CrCo_2O_4$/PPy	Hydrothermal	991.25 F g^{-1} (5 mV s^{-1}), 1600 W kg^{-1}, 97.77 W h kg^{-1}	N/A	76.75% (10k) cycle	73
$MnCo_2O_4$/MWCNTs	Co-precipitate method	540 F g^{-1} (0.5 A g^{-1}), 21 KW kg^{-1}, 58 Wh kg^{-1}	N/A	87.9% (5k) cycle	74
$CrCo_2O_4$/40%MXene	Hydrothermal	1009.12 C g^{-1} (5.8 A g^{-1}), 1470.58 W kg^{-1}, 70.08 Wh kg^{-1}	N/A	97% (3k) cycle	75
$CrCo_2O_4$/9%CNTs	Hydrothermal	817.30 C g^{-1} (1.35 A g^{-1}), 338.98 W kg^{-1}, 56.75 Wh kg^{-1}	2.65×10^{-10}	98% (10k) cycle	This work

9% exhibits a pronounced reduction in peak area in the negative region near zero potential. Sometimes, the incorporation of CNTs can also cause this type of enhanced reduction peak due to the improved ionic conductivity in that region, thereby leading to a more dominant reduction peak.[64]

GCD analysis was carried out to evaluate the charge storage performance of the device. In the two-electrode configuration, charge–discharge profiles were recorded at various current densities within an applied PW of 1.2 V for the CCO and CCO-9%. Due to the practical nature of the device setup, it exhibits relatively low internal resistance, which results in a low IR drop as depicted in Fig. 9(d) and (e). This type of GCD curve is admired due to the high conductivity attributed to the inclusion of CNTs and the porous electrode, which facilitates efficient ion transport.[65] A slight voltage drop at the discharge portion reflects a well-established E/E interface. Collectively, these features contribute to enhanced power delivery and stable cycling performance. The Q_{sp} was calculated at various J in a range of 1.6 to 8.4 A g^{-1}. The maximum Q_{sp} for pristine CCO was measured at about 98.4 C g^{-1} along with E_d and P_d of 16.41 W kg^{-1} and 1016.94 Wh kg^{-1}. While for the CCO-9%, the maximum Q_{sp} was measured as 129.48 C g^{-1}, with an E_d of 21.58 W kg^{-1}. The high power in this assembly is directly related to the low IR drop in the GCD curves. The interplay between these capacity values is depicted in Fig. 9(f) and (g).

To gain a deeper insight into the ion transport behavior, the EIS plot of CCO-9% is presented in Fig. 8(h). Based on this analysis, the R_s reduces up to zero, while the diameter of the semicircle is marginally reduced, which corresponds to the very low R_{ct}. This marginalization in R_{ct} enhances the power output, as we have observed in GCD analysis.[66,67] The prominent tail observed at low frequencies indicates that ion diffusion processes significantly influence the system, thereby contributing to the overall impedance. These observations underscore the critical insights for device fabrication and interfacial optimization in enhancing the EC performance for ESD. The reported values of all the calculated parameters are also compared with the previously published reports, as given in Table 5. Moreover, these results underscore the promising applicability of the CCO-9% composite for scalable and efficient storage solutions in real-world environments, like LED flash modules, wireless sensors, Bluetooth and wearable electronic devices.

4 Conclusion

In summary, CCO and its composite variants CCO-3%, CCO-6%, and CCO-9% were successfully synthesized through a combination of hydrothermal and solvothermal methods. Structural investigations confirmed the maintenance of the spinel cubic structure of CCO across all the samples, regardless of the CNT content. Morphological analysis *via* electron microscopy revealed spherical particles within the 200–300 nm range, exhibiting a well-dispersed configuration, while the CNTs exhibited a fibrous structure. EDX further substantiated the successful integration of CNTs within the CCO framework without any trace of foreign impurities. EC assessments indicated the dominance of a hybrid redox mechanism across all the samples *via* Dunn's model. Among the synthesized materials, CCO-9% exhibited superior EC performance, with a Q_{sp} of 817.30 C g^{-1} and an E_d of 56.75 Wh kg^{-1}. Moreover, GITT analysis revealed a large diffusion coefficient of 2.65×10^{-10} $cm^2\ s^{-1}$, highlighting its superior ionic diffusion characteristics. Furthermore, in two-electrode device testing, CCO-9% achieved a Q_{sp} of 129.48 C g^{-1}, corresponding to an E_d of 21.58 Wh kg^{-1} and a P_d of 1016.94 W kg^{-1}. The electrode demonstrated remarkable cycling stability, sustaining 98% of its initial capacity and achieving a coulombic efficiency of 97% after 10k cycles. These findings collectively establish CCO-9% as an efficient electroactive material for next-generation hybrid SCs, sensors and electronic devices.

Conflicts of interest

We declare that there are no competing/financial or any other type of interests to declare.

Data availability

The data will be available upon request.

Acknowledgements

The authors would like to acknowledge the Ongoing Research Funding Program (ORF-2026-71), King Saud University, Riyadh, Saudi Arabia.

References

1 A. Qayyum, M. O. ur Rehman, F. Ahmad, M. A. Khan, S. M. Ramay and S. Atiq, *Solid State Ionics*, 2023, **395**, 116227.
2 S. Jayakumar, P. C. Santhosh, M. M. Mohideen and A. V. Radhamani, *J. Alloys Compd.*, 2024, **976**, 173170.
3 B. K. Roy, I. Tahmid and T. U. Rashid, *J. Mater. Chem. A*, 2021, **9**, 17592–17642.
4 M. Shoeb, F. Mashkoor, H. Jeong, A. H. Anwer, S. Zhu, M. Z. Ansari and C. Jeong, *Chem. Eng. J.*, 2023, **466**, 143116.
5 Q. X. Xia, J. Fu, J. M. Yun, R. S. Mane and K. H. Kim, *RSC Adv.*, 2017, **7**, 11000–11011.
6 X. Chen, H. Ge, W. Yang, J. Liu and P. Yang, *J. Energy Storage*, 2023, **68**, 107700.
7 X. Xie, Y. Xu, J. Liu, D. Wang, T. Lv, F. Yuan and Q. Zhang, *ACS Appl. Mater. Interfaces*, 2024, **16**, 68157–68168.
8 L. Yuan, D. Fan, Y. Liu, Z. Li, C. Xu and N. Xin, *J. Electroanal. Chem.*, 2024, **975**, 118758.
9 Y. Li, L. Zheng, W. Wang and Y. Wen, *Int. J. Electrochem. Sci.*, 2020, **15**, 11567–11583.
10 Y. B. Tan and J. M. Lee, *J. Mater. Chem. A*, 2013, **1**, 14814–14843.
11 M. Luqman, M. Mehak, M. U. Salman, S. M. Ramay, M. Younis and S. Atiq, *Appl. Phys. Lett.*, 2025, **127**, 083901.
12 M. Shahid, G. M. Mustafa, A. Quader, S. M. Ramay, M. A. Shar and S. Atiq, *Diamond Relat. Mater.*, 2024, **142**, 110777.
13 S. Sahoo, G. Dhakal, W. K. Kim and J. J. Shim, *J. Mol. Liq.*, 2025, **417**, 126663.
14 M. Mehak, M. Luqman, M. U. Salman, A. Ahmad, S. M. Ramay, M. Younis and S. Atiq, *J. Mater. Chem. C*, 2025, **37**, 19067–19492.
15 X. Ge, Y. Liu, F. T. Goh, T. A. Hor, Y. Zong, P. Xiao and Z. Liu, *ACS Appl. Mater. Interfaces*, 2014, **6**, 12684–12691.
16 C. Du, Z. Zhao, H. Liu, S. Wang, Y. Hao, D. Jiang and L. Liao, *J. Energy Storage*, 2025, **106**, 114885.
17 Z. Li, R. Wu, E. Bao, S. Du, C. Xu, J. Zhu, H. Mao and H. Chen, *Ceram. Int.*, 2023, **49**, 10411–10419.
18 X. Yang, X. Jin, H. Feng, L. Tian, L. Liu, J. Ding, N. Qamar and Z. Xing, *J. Phys. Chem. Solids*, 2024, **193**, 112208.
19 S. D. Dhas, P. S. Maldar, M. D. Patil, M. R. Waikar, R. G. Sonkawade, S. K. Chakarvarti, S. K. Shinde, D. Y. Kim and A. V. Moholkar, *Mater. Sci. Eng. B*, 2021, **271**, 115298.
20 D. Shen, R. Zhang, S. Liu, H. Yu, D. Xia, J. Niu, Y. Yang, Z. Ren and W. Dong, *J. Energy Storage*, 2025, **105**, 114775.
21 R. Shafique, M. Rani, A. Mahmood, R. A. Alshgari, K. Batool, T. Yaqoob, N. K. Janjua, S. Khan, S. Khan and G. Murtaza, *Int. J. Energy Res.*, 2022, **46**, 6689–6701.
22 S. A. Kumar, T. Shahanas and G. Harichandran, *J. Energy Storage*, 2024, **77**, 110011.
23 C. V. M. Gopi, S. Alzahmi, M. Y. Al-Haik, Y. A. Kumar, F. Hamed, Y. Haik and I. M. Obaidat, *Mater. Today Sustainability*, 2024, **28**, 100981.
24 M. Sadiq, M. A. Khan, M. Sarvar, M. M. H. Raza, S. M. Aalam, M. Zulfequar and J. Ali, *Hybrid Adv.*, 2023, **3**, 100051.
25 M. S. Ratsoma, B. L. Poho, K. Makgopa, K. Raju, K. D. Modibane, C. J. Jafta and K. O. Oyedotun, *J. Electron. Mater.*, 2023, **52**, 2264–2291.
26 T. Zhao, C. Hou, H. Zhang, R. Zhu, S. She, J. Wang, T. Li, Z. Liu and B. Wei, *Sci. Rep.*, 2014, **4**, 5619.
27 M. A. Khan, G. M. Mustafa, S. Riaz, M. Saleem and S. Atiq, *Ceram. Int.*, 2023, **49**, 22576–22585.
28 L. Blaubaum, F. Roder, C. Nowak, H. S. Chan, A. Kwade and U. Krewer, *ChemElectroChem*, 2020, **7**, 4755–4766.
29 Q. Kuang, X. Wang, Z. Jiang, Z. Xie and L. Zheng, *Acc. Chem. Res.*, 2014, **47**, 308–318.
30 G. Wee, O. Larsson, M. Srinivasan, M. Berggren, X. Crispin and S. Mhaisalkar, *Adv. Funct. Mater.*, 2010, **20**, 4344–4350.
31 S. Guo, E. R. Meshot, T. Kuykendall, S. Cabrini and F. Fornasiero, *Adv. Mater.*, 2015, **27**, 5726–5737.
32 Z. Li, D. Guo, D. Wang, M. Sun and H. Sun, *J. Power Sources*, 2021, **506**, 230197.
33 M. M. Gul and K. S. Ahmad, *Int. J. Energy Res.*, 2022, **46**, 18697–18710.
34 M. A. Aziz, S. S. Shah, Y. A. Mahnashi, W. Mahfoz, A. S. Alzahrani, A. S. Hakeem and M. N. Shaikh, *Small*, 2023, **19**, 2300258.
35 M. Zhou, F. Li, J. Dong, S. Sun, Y. Zhu, W. Zhang and Y. Huang, *Adv. Compos. Hybrid Mater.*, 2024, **7**, 136.
36 A. Kumar, A. Pandurangan, S. Arumugam and M. Sathiskumar, *Sci. Rep.*, 2019, **9**, 1228.
37 L. Hu, D. Guo, G. Feng, H. Li and T. Zhai, *J. Phys. Chem. C*, 2016, **120**, 24675–24681.
38 L. Guan, L. Yu and G. Z. Chen, *Electrochim. Acta*, 2016, **206**, 464–478.
39 R. Tang, M. Yamamoto, K. Nomura, E. Morallón, D. Cazorla-Amorós, H. Nishihara and T. Kyotani, *J. Power Sources*, 2020, **457**, 228042.
40 Y. Tian, C. Yang, X. Song, J. Liu, L. Zhao, P. Zhang and L. Gao, *Chem. Eng. J.*, 2019, **374**, 59–67.
41 U. Samukaite-Bubniene, A. Valiūnienė, V. Bucinskas, P. Genys, V. Ratautaite, A. Ramanaviciene and A. Ramanavicius, *Colloids Surf., A*, 2021, **610**, 125750.
42 J. Liu, P. Du, Q. Wang, D. Liu and P. Liu, *Electrochim. Acta*, 2019, **305**, 175–186.
43 M. Z. Iqbal, H. Tariq, A. Zakir, A. Khizar, A. Kumar and M. A. Khan, *J. Phys. Chem. Solids*, 2025, **197**, 112425.
44 A. M. Afzal, N. Muzaffar, M. W. Iqbal, G. Dastgeer, A. Manzoor, M. Razaq and S. M. Eldin, *J. Appl. Electrochem.*, 2024, **54**, 65–76.
45 M. Z. Iqbal, M. M. Faisal, S. R. Ali, A. M. Afzal, M. R. A. Karim, M. A. Kamran and T. Alharbi, *Ceram. Int.*, 2020, **46**, 10203–10214.

46 R. Kumar and M. Bag, *J. Phys. Chem. C*, 2021, **125**, 16946–16954.
47 J. Wang, J. Polleux, J. Lim and B. Dunn, *J. Phys. Chem. C*, 2007, **111**, 14925–14931.
48 I. Khalil, M. Mehak, M. Luqman, M. Nadeem, S. M. Ramay, M. T. Akhter and S. Atiq, *Nanoscale Adv.*, 2026, **8**, 989–1004.
49 A. K. Das, S. K. Karan and B. B. Khatua, *Electrochim. Acta*, 2015, **180**, 1–15.
50 J. Huang, B. G. Sumpter and V. Meunier, *Chem. – Eur. J.*, 2008, **14**, 6614–6626.
51 K. Surya and M. S. Michael, *J. Mater. Sci.: Mater. Electron.*, 2022, **33**, 3139–3150.
52 M. S. Iyer and I. Rajangam, *J. Energy Storage*, 2023, **67**, 107530.
53 D. W. Dees, S. Kawauchi, D. P. Abraham and J. Prakash, *J. Power Sources*, 2009, **189**, 263–268.
54 B. Han, Z. Yang, X. Shi and X. Yu, *J. Mater. Eng. Perform.*, 2013, **22**, 184–189.
55 A. V. Eletskii, A. A. Knizhnik, B. V. E. Potapkin and J. M. Kenny, *Phys.-Usp.*, 2015, **58**, 209.
56 R. Kötz, M. Hahn and R. Gallay, *J. Power Sources*, 2006, **154**, 550–555.
57 K. Li, Y. Luo, Z. Yu, M. Deng, D. Li and Q. Meng, *Electrochem. Commun.*, 2009, **11**, 1346–1349.
58 V. K. Mariappan, K. Krishnamoorthy, P. Pazhamalai, S. Sahoo and S. Kim, *Electrochim. Acta*, 2018, **265**, 514–522.
59 M. A. Zabara, G. Katırcı, F. E. Civan, A. Yürüm, S. A. Gürsel and B. Ülgüt, *Electrochim. Acta*, 2024, **485**, 144080.
60 J. P. Baboo, E. Jakubczyk, M. A. Yatoo, M. Phillips, S. Grabe, M. Dent, S. J. Hinder, J. F. Watts and C. Lekakou, *J. Power Sources*, 2023, **561**, 232762.
61 A. Noori, M. F. El-Kady, M. S. Rahmanifar, R. B. Kaner and M. F. Mousavi, *Chem. Soc. Rev.*, 2019, **48**, 1272–1341.
62 X. Li, M. Chen, L. Wang, H. Xu, J. Zhong, M. Zhang, Y. Wang, Q. Zhang, L. Mei, T. Wang, J. Zhu, B. Lu and X. Duan, *Nanoscale Horiz.*, 2020, **5**, 1586–1595.
63 B. Pal, K. J. Sarkar, B. Wu, L. Děkanovský, V. Mazánek, R. Jose and Z. Sofer, *ACS Omega*, 2023, **8**, 2629–2638.
64 G. Khan, M. Luqman, M. Mehak, M. U. Salman, A. Mehmood, W. Al-Marsry, M. Nawaz and S. Atiq, *J. Power Sources*, 2025, **660**, 238568.
65 H. Shao, Y. C. Wu, Z. Lin, P. L. Taberna and P. Simon, *Chem. Soc. Rev.*, 2020, **49**, 3005–3039.
66 A. A. Ambalkar, U. V. Kawade, Y. A. Sethi, S. C. Kanade, M. V. Kulkarni, P. V. Adhyapak and B. B. Kale, *RSC Adv.*, 2021, **11**, 19531–19540.
67 C. Harak, V. Kadam, R. Gavhane, S. Balgude, A. Rakshe, N. Brahmankar, S. Uke, D. Satpute, H. Pawar and S. Mardikar, *RSC Adv.*, 2024, **14**, 4917–4929.
68 S. Xu, D. Yang, F. Zhang, J. Liu, A. Guo and F. Hou, *RSC Adv.*, 2015, **5**, 74032–74039.
69 S. Zawae, G. Ali, G. M. Mustafa, S. A. Patil, S. M. Ramay and S. Atiq, *J. Energy Storage*, 2022, **50**, 104298.
70 P. Wu, S. Cheng, M. Yao, L. Yang, Y. Zhu, P. Liu and M. Liu, *Adv. Funct. Mater.*, 2017, **27**, 1702160.
71 A. Razzaq, A. Kumar, A. M. Afzal, B. Kanabar, S. Ballal, M. Al-Sabah, K. Jayabalan, S. Samantaray, H. Karamti, S. Kaushal and A. D. Oza, *J. Mater. Sci.: Mater. Electron.*, 2025, **36**, 1578.
72 A. Chebil, O. Kuzgun, C. Dridi and M. Ates, *Ionics*, 2020, **26**, 5725–5735.
73 S. Kour, P. Kour and A. L. Sharma, *Nanoscale*, 2024, **16**, 21456–21470.
74 S. K. Mittal, S. Saini, U. Jamwal, D. Yadav, D. Kaneria and K. L. Yadav, *J. Phys. Chem. C*, 2024, **129**, 61–74.
75 M. Luqman, M. Mehak, M. U. Salman, A. Raza, S. M. Ramay, M. Younis and S. Atiq, *J. Power Sources*, 2025, **655**, 237943.